Advances in Quantitative Muscle Ultrasonography Using Texture Analysis of Ultrasound Images

Advances in quantitative muscle ultrasonography using texture analysis of ultrasound images

Filippo Molinari [1], Cristina Caresio [1,2], U. Rajendra Acharya [3,4], Muthu Rama Krishnan Mookiah [3], and Marco Alessandro Minetto [2,5]

[1]Biolab, Department of Electronics and Telecommunications, Politecnico di Torino, Turin, Italy

[2]Division of Endocrinology, Diabetology and Metabolism, Department of Medical Sciences, University of Turin, Turin, Italy

[3]Department of Electronics and Computer Engineering, Ngee Ann Polytechnic, Singapore

[4]Department of Biomedical Engineering, SIM University, Singapore.

[5]Division of Physical Medicine and Rehabilitation, Department of Surgical Sciences, University of Turin, Turin, Italy

SHORT TITLE

Muscle ultrasonography texture analysis

CORRESPONDING AUTHOR

Prof. Filippo Molinari, PhD

Biolab, Department of Electronics and Telecommunications, Politecnico di Torino, Torino, Italy.

Corso Duca degli Abruzzi, 24 - 10129 Torino, ITALY

Phone: 0039 011 090 4153

Fax: 0039 011 090 4217

E-mail: filippo.molinari@polito.it

ABSTRACT

Muscoloskeletal ultrasound imaging can be used to investigate the skeletal muscle structure in terms of architecture (thickness, cross sectional area, fascicle length, and fascicle pennation angle) and texture. Gray-scale analysis is commonly used to characterize transverse scans of the muscle. Gray mean value is used to distinguish between normal and pathological muscles, but it depends on the image acquisition system and its settings.

In this study, quantitative ultrasonography was performed on five muscles (biceps brachii, vastus lateralis, rectus femoris, medial gastrocnemius, and tibialis anterior) of twenty healthy subjects (10 females, 10 males) to assess the characterization performance of higher-order texture descriptors to differentiate genders and muscle types. A total of 53 features (7 first-order descriptors, 24 Haralick features, 20 Galloway features, and 2 Local Binary Pattern features) were extracted from each muscle region of interest (ROI) and were used to perform the multivariate linear regression analysis (MANOVA). Our results show that first order descriptors, Haralick features (energy, entropy, and correlation measured along different angles) and local binary pattern (LBP) energy and entropy were highly linked to the gender, whereas Haralick entropy and symmetry, Galloway texture descriptors, and LBP entropy helped to distinguish muscle types. Hence, the combination of first-order and higher-order texture descriptors (Haralick, Galloway, and LBP) can be used to discriminate gender and muscle types. Therefore, multi-texture analysis may be useful to investigate muscle damage and myopathic disorders.

Keywords: Muscle ultrasonography, texture analysis, muscle characterization, musculoskeletal ultrasound, Haralick features, Galloway features, Local Binary Pattern, gray scale mean value, MANOVA

INTRODUCTION

Ultrasound imaging is proven to be effective in the investigation of the skeletal muscle structure (Walker et al. 2004; Pillen et al. 2008; Pillen and van Alfen 2011). The main advantages of ultrasounds are portability, low associated costs of the examination, and non-invasivity of the method. Moreover, the acoustic power levels used in diagnostic equipment minimize the probability of biological negative effects. Ultrasound imaging is however an operator-dependent technique. In order to lower the intra- and inter-reader variability, quantitative approach is needed.

The quantitative features most commonly extracted from ultrasound images to investigate muscle size are cross sectional area, thickness, fascicle length, and fascicle pennation angle (Narici et al. 1996; Chow et al. 2000; Reeves et al. 2004). The muscle quality is commonly assessed through the quantification of the mean echo intensity by gray-scale analysis of a region of interest (ROI). This numerical parameter is highly dependent on the ultrasound scanner settings (Zaidman et al. 2008; Pillen et al. 2009b).

Contrary to the mean echo intensity and other first order descriptors, higher-order texture features that can be extracted from ultrasound images are intensity invariant (Acharya et al. 2012d; Acharya et al. 2012e; Acharya et al. 2012f), and have already proven informative in the analysis of intramuscular fat content in animals (Kim et al. 1998), as well as in the characterization of arterial surface roughness (Acharya et al. 2012a; Niu et al. 2013), breast (Singh and Singh 2010) and ovarian tumors (Acharya et al. 2012c; Acharya et al. 2013), thyroid lesions (Acharya et al. 2012b; Acharya et al. 2014a), and liver images (Gao et al. 2014; Acharya et al. 2015) in human studies. Moreover, in a recent review focused on thyroid cancer, Acharya *et al.* showed that high characterization performance can be achieved only when sonographic features from the ultrasound images are merged to non-clinical features extracted from the ultrasound images using statistical and data mining techniques (Acharya et al. 2014b). They have also showed that higher-order and non-linear descriptors offer better characterization performance than histogram-based parameters (Acharya et al. 2012c; Acharya et al. 2014b).

To the best of our knowledge, in previous studies, only linear and first-order descriptors are used to characterize the texture of different skeletal muscles. In this paper, we characterized the image texture of five skeletal muscles of healthy men and women using different texture features. We show that Haralick features (second order statistical descriptors), Galloway features, and texture descriptors based on the Local Binary Pattern (LBP) are unique for gender and muscle type. It can be seen from our results that the texture features are superior to the first order descriptors (based on the echo intensity histogram) in classifying the muscle type.

METHODS

Subjects

Twenty healthy volunteers (10 females: age 26.0 ± 2.3 years; body mass index 20.7 ± 2.2 kg/m^2 and 10 males, age 30.2 ± 5.6 years; body mass index 23.3 ± 2.6 kg/m^2) participated in this study. Health status was assessed by medical history, clinical exam, and electrocardiogram. The "Waterloo Handedness and Footedness Questionnaires - Revised" (Elias et al. 1998) was used to assess side dominance. Among them, three subjects were left side dominant. Before participating in the study, the subjects were instructed about the aims and then they signed a written informed consent. The study conformed to the guidelines of the Declaration of Helsinki and was approved by the local ethical committee.

Ultrasound procedures and equipment

During a single experimental session, we acquired ultrasound B-mode images of the following five muscles from each subject: biceps brachii, vastus lateralis, rectus femoris, medial gastrocnemius, and tibialis anterior. Images were acquired on both sides of the subjects.

The same experienced sonographer (MAM) conducted the clinical examinations and acquired all the images. Three consecutive scans were acquired in the transverse plane of each muscle. After each scan, the subject moved and then the transducer was repositioned. To increase the repeatability of the acquisitions and to ensure that the insonation was orthogonal to the bone, the optimal insonation angle was selected by maximizing the representation of the bone boundary.

The medial gastrocnemius was insonated with the subjects in prone position, whereas for all other muscles the supine position was maintained. In all measurements, the arms and legs were extended and the subjects were asked to completely relax their muscles. Ultrasound coupling gel (Ultrasound transmission gel, REF: 907137475, PBpharma, Torino, Italy) was used to ensure optimal image quality while limiting the transducer pressure on the skin. All scans were performed by placing the transducer in correspondence to the largest muscle diameter at the following anatomical sites: the

biceps brachii was measured at two-thirds of the distance from the acromion to the antecubital crease; the rectus femoris halfway along the line from the anterior-superior iliac spine to the superior border of the patella; the vastus lateralis halfway along the line from the anterior-superior iliac spine to the superolateral border of the patella; the tibialis anterior at one-quarter of the distance from the inferior border of the patella to the lateral malleolus; the medial gastrocnemius from the mid-sagittal line of the muscle, midway between the proximal and distal tendon insertions.

We used a MyLab™ Twice ultrasound device (Esaote, Genoa, Italy) equipped by a linear-array transducer (code LA533) with a bandwidth from 3 to 13 MHz. Gain was set at 50% of the range, dynamic image compression was turned off, and time gain compensation was maintained in the same (neutral) position for all depths. All system-setting parameters were kept constant throughout the study for each subject. The depth setting (initially set at 44 mm) was adapted for each subject during examination in order to display the entire muscle. The conversion factor was equal to 0.92 mm/pixel. The pictures in DICOM format were transferred to a computer for offline processing.

Texture feature extraction

All images were visually inspected and analyzed by the same experienced operator (CC), who positioned a ROI in each image as shown in fig. 1. One ROI was chosen in the median portion of the biceps brachii, vastus lateralis, and medial gastrocnemius, while two equal sized ROIs were chosen in the rectus femoris (fig. 1.A) and tibialis anterior (fig. 1.C) to include most of the muscle without the central aponeurosis (white arrow in fig. 1.A) and the internal fascia (white arrow in fig. 1.C). Figure 1.B depicts the ROI positioning for the vastus lateralis and fig. 1.D for the medial gastrocnemius. The two ROIs of the rectus femoris are indicated as medialis and lateralis and abbreviated as RF_{Med} and RF_{Lat}, respectively. The tibialis anterior ROIs are indicated as superior and inferior and abbreviated as TA_{Sup} and TA_{Inf}, respectively. The dimension and the position of the ROIs were chosen to be the same for each muscle of all subjects in order to make the extracted features independent of ROI size. The following ROI areas were considered for each muscle: 286

mm^2 for the biceps brachii, 144 mm^2 for the rectus femoris, 338 mm^2 for the vastus lateralis, 68 mm^2 for the tibialis anterior, 338 mm^2 for the medial gastrocnemius.

Different features extracted from the ROIs are described in the following. The mean of six measurements (one measurement per ROI for both sides) was used for comparison among muscles and between genders. All the texture parameters were computed by custom developed software in MATLAB (The MathWorks, Natick, MA, USA).

First order statistical descriptors

Based on the first order statistics, the following seven features were extracted from the image ROIs: integrated optical density, mean, standard deviation, variance, skewness, kurtosis and energy. Table 1 presents the mathematical description of these features. The energy feature is denoted as $Energy_1$ to avoid confusion with the same second order parameter (described in the next section).

Haralick features

The Haralick features (also called second order statistical descriptors) are based on the Gray Level Co-occurrence Matrix (GLCM) (Haralick et al. 1973). The GLCM is a square matrix with dimension equal to the number of gray levels in the image. Let *C* be the matrix containing the GLCM. The element *C(i,j)* measures the number of times in which a pixel of given gray level *i* is found adjacent to a pixel of gray level *j*. Since two pixels can be adjacent in vertical, horizontal and in the two diagonal directions, we computed *C(i,j)* for the four angles 0º, 45º, 90º, and 135º. Figure 2 shows an example of construction of the GLCM for the horizontal direction: fig. 2.A depicts the numerical values representing the pixels of an image that is rendered in a linear gray scale in fig. 2.C. The corresponding GLCM is numerically computed in fig. 2.B and the gray scale representation of the GLCM is shown in fig. 2.D. The red circles in fig. 2.A indicate the horizontal adjacencies of the pixel $i = 1$ and of the pixel $j = 6$. There are four occurrences of this adjacency, hence the corresponding pixel *C(1,6)* in fig. 2.B has a value equal to 4.

The Haralick features are the mathematical descriptors of the GLCM (fig. 2.D). We computed the following six features: symmetry, contrast, homogeneity, entropy, energy, and correlation. Since each feature is computed along 4 angular directions, we have 24 descriptors per ROI. These second order features are mathematically defined in Table 2. The full mathematical details about the Haralick features are reported in Appendix.

Galloway features

The Galloway features (Galloway 1975) are based on the run length matrix (RLM) *R*. In a RLM, the pixel *R(i,j)* contains the number of pixels with run length *j* and intensity *i* in a given direction. The RLM has a number of rows equal to the number of gray levels in the image and a number of columns equal to the maximum length of the run length. Galloway (Galloway 1975) observed that in coarse texture, long gray level runs may exist more frequently as compared to fine texture which generally contains short runs. This means that we expect longer sequences of pixels with same intensity in coarse images, but only short runs in fine textures. The Galloway features are then mathematical descriptors of the runs of the RLM: short run emphasis, long run emphasis, gray-level non-uniformity, run length non-uniformity, and run percentage. Table 3 reports the mathematical description of the features that were calculated from the RLM. Since each feature was computed along four different angles (0º, 45º, 90º, and 135º), we have extracted 20 Galloway features per ROI.

Local Binary Pattern features

The Local Binary Pattern (LBP) was introduced by Ojala *et al.* in the field of texture analysis and face recognition (Ojala et al. 1996; Ojala et al. 2002). Basically, by means of this technique, a LBP value is assigned to a pixel neighborhood on the basis of the comparison of the pixels' intensities with the intensity of the central pixel. With reference to fig. 3, let's consider the central pixel of the 3x3 neighborhood in fig. 3.A. The intensity of the central pixel is used to threshold the

neighborhood and a pixel is assigned the value 0 if its intensity is lower than the center or 1 otherwise (fig. 3.B). Then, the binarized image is multiplied by the image containing the powers of 2 (fig. 3.C) and the resulting image (fig. 3.D) is used to compute the LPB, which is the sum of all the pixels (in the case of fig. 3.D the LBP is equal to 216). Hence, each pixel is assigned a LBP value. Acharya *et al.* demonstrated that two powerful descriptors of the LBP image are the energy and entropy of the LBP distribution (Acharya et al. 2012d). Particularly, the indicators based on LBP have lower values for more homogeneous images, and assume higher values for more inhomogeneous images. The full mathematical details of the LBP computation method we adopted are reported in the Appendix.

Statistical analysis and classification

The *Shapiro-Wilk* test was used to assess the normality of the variable distributions. Normally distributed data were analysed using the Student's t-test, while non-normally distributed data were analysed using the Mann-Whitney U test. The Kruskal-Wallis ANOVA (followed by Dunn's post-hoc test) was adopted for comparing the features' value among the different muscles.

The overall number of texture descriptors was equal to 53 per ROI (7 first-order descriptors, 24 Haralick features, 20 Galloway features, and 2 LBP features). Since we had 5 muscles and 7 ROIs (the RF and TA were measured in two different ROIs), and since we measured the dominant and non-dominant side, each subject was represented by 742 features. Multivariate analysis of variance (MANOVA) was used to test the equality of the means among groups. We tested the texture feature values against gender and against the muscle type. To avoid singularities in the observation matrix, prior to performing the MANOVA analysis, collinear variables were removed by computing the *Wilks' Lambda*, which is defined as the ratio between the determinant of the *within* group variance matrix and the sum between the determinants of the *within* and *between* matrices. Conceptually, the *Wilks' lambda* is the proportion of the total variance in the discriminant scores not explained by differences among the groups The *Lambda* ranges from 0 to 1 and the lower is the value, the more

discriminant between groups is the associated variable (Costanza and Afifi 1979). The optimal *Lambda* value for our dataset was found to be 0.35. Higher values lead to insufficient removal of collinear variables, whereas lower values discarded an excessive number of variables. The dimension of the MANOVA was used to assess the number of groups the data belong to. For example, a dimension equal to zero indicates that it is not possible to reject the hypothesis that all the subjects belong to the same group, whereas a dimension equal to 1 indicates that the subjects can be divided into two groups. Classification of the subjects on the basis of either the gender or muscle type was obtained by linear regression analysis performed on the most significant features, as revealed by MANOVA. All the continuous data variables were represented by means ± standard deviation (SD). The statistical significance is set to P = *0.05*. Statistical analyses were performed by R (www.**r**-project.org) and MATLAB.

RESULTS

Comparisons between sides and genders

All the texture features of the dominant side were correlated to the non-dominant side ($P < 0.001$). The lowest value of the *Wilks' Lambda* was 0.875. Accordingly, the MANOVA analysis was not significant when the side dominance was the dependent variable. Therefore, we averaged the variables of the two sides: the total number of variables was equal to 371 for each of the subjects.

When the gender was considered as the dependent variable, after removing the collinear variables, 38 features were left. The MANOVA dimension of the group means was equal to 1 ($P < 0.001$). The dimensionality of the MANOVA was important to understand how samples were distributed on the hyperplane of the canonical variables. The canonical variables are linear combinations of the original features and are built in order to maximize the variance among groups. Since the canonical variables are ordered with decreasing explained variance, the dimension of 1 ensured that only one canonical variable (the first) is enough to separate the subjects on the basis of gender. We plotted the 1st and 2nd canonical variable for each subject (fig. 4) and we indicated the males by a full symbol (circle) and females by an empty one, and kept the same notation throughout the paper. The graph demonstrates that the first canonical variable was discriminant for gender. The left column of Table 4 reports the ten variables (*i.e.*, the image features) with highest weight on the first canonical variable (i.e., the most discriminant between the two genders). First order and Galloway features were not significant ($P > 0.2$). Haralick features (energy, entropy, and correlation), LBP energy and entropy were significantly higher (Haralick energy, $P < 0.01$) and lower (all other features, $P < 0.001$) in males compared to females (fig. 5). By using those ten most discriminant features, we performed a classification of the subjects based on the linear regression. All the subjects were correctly classified, with sensitivity and specificity of 100% (correlation coefficient equal to 1 and 95% confidence interval 0.98-1) and an area under the receiving-operator-curve (AUROC) equal to 1.

Comparison among muscles

When the muscle was considered as the dependent variable, after removing the collinear variables, 43 features were left. The MANOVA dimension was equal to 6 ($P<0.02$), thus we could consider that samples belonged to 7 different groups. Figure 6.A shows the different muscles plotted in the plane of the first two canonical variables, whereas fig. 6.B shows the same distribution in the plane of the first and third canonical variables. The right column of Table 4 reports the ten original features that were most discriminant among the different muscles. The most important features were the Galloway ones (gray-level non-uniformity, run length non-uniformity, run percentage, short run emphasis), the Haralick ones (entropy and symmetry) and the $LBP_{entropy}$. No first order features are listed. Figure 7 shows the gray-level non-uniformity (GLNU, fig. 7.A), the run length non-uniformity (RLNU, fig. 7.B), the $LBP_{entropy}$ (fig. 7.C) and the Haralick entropy (fig. 7.D) for the different muscles and ROIs. No significant difference in the texture features was observed between the different ROIs selected in the rectus femoris and tibialis anterior muscles ($P > 0.05$ for all comparisons). Galloway features (GLNU and RLNU) and the Haralick entropy resulted higher ($P < 0.05$ for all comparisons) in biceps brachii, medial gastrocnemius, and vastus lateralis muscles in comparison to rectus femoris and tibialis anterior muscles. It can be noticed that the texture descriptors considered alone do not have a very high discriminatory power.

The performance in classifying different muscles using the linear regression is reported in Table 5 (leftmost half). The average sensitivity was equal to 76.4 ± 21.9%, the specificity to 97.7 ± 1.9%, the correlation coefficient was 0.98 (95% confidence interval 0.93-1), and the AUROC to 0.976 ± 0.026. The two ROIs of the tibialis anterior were perfectly classified (AUROC=1), and the worst performance was obtained in classifying the rectus femoris (AUROC=0.936).

Comparisons between genders and among muscles based on the first order descriptors

To further compare the performance of the Haralick, Galloway, and LBP features with the first order descriptors, we performed the MANOVA analysis and the classification using only the 7 first

order features. Figure 8.A represents the subjects on the basis of the gender as returned by the first two canonical variables of the MANOVA analysis. The dimension obtained by the MANOVA was 1 ($P < 0.02$), thus allowing for the separation of the samples in two groups. A distinction of the two groups is still evident, even though not defined as in fig. 4 for Haralick and LBP features. Accordingly, the first order features were significantly different between males and females. It can be seen from fig. 9 that the mean echo intensity of four muscles was higher for females than males. When we classified the subjects on the basis of the gender using only the 7 first order features, we obtained a 100% sensitivity and specificity and an AUROC equal to 1. Hence, the use of Haralick and LBP features did not improve the description of subjects on the basis of gender.

Similarly, we classified the muscles using only the 7 first order descriptors and we did not get clear separation among the muscles (fig. 8.B). As the muscles are not separated as in fig. 6, we expected a lower classification performance when first order descriptors were used to differentiate among the five muscles. The dimension obtained by the MANOVA was 6 ($P < 0.05$). The rightmost part of Table 5 reports the classification performance we obtained when the linear regression was performed using the 7 first order features. The average sensitivity of 46.4 ± 32.3%, the specificity of 97.3 ± 1.92%, and AUROC of 0.907 ± 0.081 was obtained. The sensitivity and the AUROC were significantly ($P < 0.01$) lower than Haralick, Galloway, and LBP features. Consistently, the first order features resulted statistically comparable among the five muscles ($P > 0.05$). In other words, the overall performance was lower than when higher-order descriptors were used, but this decreased performance was consistent for all the muscles.

Briefly, it was possible to differentiate between the two genders on the basis of the first order descriptors, while the Haralick, Galloway, and LBP features classified the images of different muscles with a better performance than the first order features.

DISCUSSION

In the present study, quantitative ultrasonography was performed in five muscles (biceps brachii, rectus femoris, vastus lateralis, tibialis anterior, medial gastrocnemius) of twenty healthy subjects to assess the characterization performance of higher-order texture descriptors in the differentiation between genders and among muscles. Our results show that first order descriptors, Haralick features (energy, entropy, and correlation measured along different angles), LBP energy and entropy were highly linked to the gender, whereas Haralick entropy and symmetry, Galloway texture descriptors, and LBP entropy helped to distinguish different types of muscles. To the best of our knowledge, this is the first study that used higher-order textural descriptors to characterize the human muscles using ultrasound images.

Previous studies have shown that the first order descriptors (i.e., mean or median echo intensity) help to study the echogenicity of different genders and skeletal muscles (Arts et al. 2010), and muscle adaptations to physical training (Radaelli et al. 2012). Moreover, muscle echo intensity quantification enables to characterize the disruption of the normal structure that occur in both myopathic and neuropathic and damaged muscles. Neuromuscular disorders and myopathic conditions are associated to fat and collagen infiltration (Pillen et al. 2008; Arts et al. 2010) and/or interstitial edema (Fujikake et al. 2009). These histologic changes increase the reflection of the ultrasound beam and result in increased echo intensity (Walker et al. 2004; Pillen et al. 2008).

Despite these results, the muscle echo intensity presents a major criticism that limits its clinical use: it is dependent on the settings of the ultrasound scanner and is therefore different for each ultrasound device used. To improve the reproducibility of the echo intensity, Zaidman *et al.* studied a calibration procedure (Zaidman et al. 2008; Zaidman et al. 2012) and proposed a calibrated muscle backscatter index, which was adopted in the analysis of muscular dystrophy (Zaidman et al. 2010). The need for a calibration procedure is, however, impractical in the clinical environment. Also, as shown by authors, the quality of the calibration depends on the ROI size and location

inside the muscle (Zaidman et al. 2012). Another approach for the comparison of echo intensity values between different ultrasound devices was proposed by Pillen et al. (Pillen et al. 2009b) who adopted a conversion equation (based on standardized measurements of the same samples made with two ultrasound devices) to transpose the echo intensity values obtained with one device to another device.

Another criticism of the muscle echo intensity is that it is able to capture only the overall change in the brightness of the muscle, but it cannot measure the actual texture. Few studies have attempted to develop quantification methods that can overcome the limitation of echo intensity in measuring the image texture. Maurits *et al.* proposed quantitative variables obtained by density analysis (such as muscle inhomogeneity and white-area index, which measures the presence of patches of high echogenicity) to differentiate between myopathies and neuropathies (Maurits et al. 2003) and to distinguish between healthy muscles and neuromuscular diseases (Maurits et al. 2004). The rationale was that highly inhomogeneous muscles showed a higher number of bright pixels in the gradient compared to homogeneous muscles. The white-area index is anyway correlated to the overall brightness of the ultrasound image; thus, it suffers from the same limitations of the mean echo intensity. Gdynia *et al.* used the muscle echo intensity, the first order entropy, and the fractal dimension to analyze the ultrasound images of tibialis anterior and medial gastrocnemius muscles of healthy subjects and patients affected by myopathies and motor neuron disorders (Gdynia et al. 2009). They showed that the parameters were able to distinguish between healthy and pathological muscles, but not between muscles affected by different pathologies. Entropy filtering, combined with vibration elastography was used in another study on the myofascial trigger points of the upper trapezius muscle (Turo et al. 2013). The combination of the two measurements lead to overall good performance (sensitivity of about 70% and specificity of 80%) in discriminating myofascial trigger points from normal tissue. Both the studies showed that entropy analysis can extract more information from the B-mode images than the mean echo intensity. However, the measurement of the first order entropy is based on the intensity histogram distribution of the pixels. Thus, the

texture information present in the image and reflecting the muscle microstructure is not fully captured.

On the contrary, the image texture analysis enables to overcome both limitations of the first order descriptors (Acharya et al. 2012a; Acharya et al. 2012b; Acharya et al. 2012c). In the present study, we used both first order descriptors and higher-order texture descriptors to discriminate between genders and different skeletal muscles of healthy subjects.

The main findings of this study are the following:

i) First order and texture descriptors are comparable to the dominant and non-dominant side of each muscle.

ii) First order features help to distinguish the two genders.

iii) Galloway features, quantify the coarseness of an image along a given direction (i.e., describe the spatial changes in the local acoustic impedance of the tissues) and enable to distinguish different types of muscles.

iv) Haralick and LBP features (in particular, Haralick entropy and LBP entropy) quantify the overall (Haralick entropy) and local (LBP entropy) image homogeneity, and distinguish both gender and muscle types.

A previous study on the echo-intensity of the tibialis anterior and of the upper limb muscles showed that the first-order descriptors had different values in the dominant and non-dominant side (Arts et al. 2010). In our study, the first order descriptors failed to differentiate between the dominant and non-dominant. Hence, further studies are required to examine the dependence of muscle echo intensity (and texture as well) on the side dominance.

Our observation of females indicating higher echo intensity compared to males is in agreement with previous findings (Arts et al. 2010; Caresio et al. 2014). But the observation that the image homogeneity (as quantified by Haralick and LBP features) is lower in females compared to males and directional coarseness (as quantified by Galloway features) difference among muscles is the original contribution of this study. Although no muscle biopsies were performed in this study, the

observed gender variability in first order descriptors, Haralick features, and LBP features may be related to the higher degree of fibrous and adipose tissue present in muscles of females compared to males (Pillen et al. 2009a; Caresio et al. 2014). The inter-muscle variability in directional coarseness probably resulted from different proportions of fibrous tissue and/or from different architectural features of the fascicles (i.e., their lengths, their arrangement relative to one another and their alignment relative to the force-generating axis). Given these possible relations between textural features and adipose and fibrous tissue content and distribution, future studies are required to investigate the type of textural features that enable to detect differences between healthy and pathological muscles. For example, conditions associated to interstitial edema in a first phase and collagen infiltration in a subsequent phase (e.g., muscle injuries) can be longitudinally assessed by quantitative muscle ultrasonography for monitoring and prognosis of the myopatic process. We found in a series of endocrine patients affected by steroid myopathy that the muscle texture impairment occurs earlier than the muscle size reduction (unpublished observations). Therefore, we infer that quantitative muscle ultrasonography has the potential to predict the occurrence (and the evolution) of a myopathic process. Moreover, we strongly feel that combinations of different texture features may be required for prediction, diagnosis, monitoring, and prognosis of the myopathic disorders.

This work has the following two main limitations. From the practical point of view, this feature-based characterization is currently still not available in commercial scanners. However, since the computation of the features is not very demanding, it is likely that applications for the characterization of images based on higher order features will be embedded in high-end scanners in a close future. A second limitation is relative to the actual capability of detecting and grading pathological conditions by using this multi-features approach. This study is methodological and aimed at demonstrating the higher sensitivity of higher order features compared to the first order ones in characterizing the different muscles. We are currently performing human investigations focused on the quantification of sarcopenia and myosteatosis based on this technique.

CONCLUSION

We have proposed a texture-based technique to differentiate gender and muscle types. In this work, we found that the combination of first-order and higher-order texture descriptors (Haralick, Galloway, and LBP) help to discriminate gender and muscle type. The most important features included entropy, since the local or global homogeneity of the image is clinically correlated to the physiological muscle status. The presented technique is objective, non-invasive, and the preliminary results indicate the possibility of using this technique to differentiate gender and muscle types. Hence, in future multi-texture analysis can be used to study the muscle damage and myopathic disorders.

ACKNOWLEDGEMENTS

This study was supported by the bank foundation “Fondazione CARIPLO” of Milano, Italy (Project: “Steroid myopathy: Molecular, Histopathological, and Electrophysiological Characterization”) and by a grant (ex 60%) from the University of Turin.

CONFLICTS OF INTEREST

The authors have no conflicts of interest.

REFERENCES

Acharya RU, Faust O, Alvin AP, Sree SV, Molinari F, Saba L, Nicolaides A, Suri JS. Symptomatic vs. asymptomatic plaque classification in carotid ultrasound. Journal of medical systems 2012a;36:1861-71.

Acharya UR, Faust O, Molinari F, Sree SV, Junnarkar SP, Sudarshan V. Ultrasound-based tissue characterization and classification of fatty liver disease: A screening and diagnostic paradigm. Knowledge-Based Systems 2015;75:66-77.

Acharya UR, Faust O, Sree SV, Molinari F, Suri JS. ThyroScreen system: high resolution ultrasound thyroid image characterization into benign and malignant classes using novel combination of texture and discrete wavelet transform. Computer methods and programs in biomedicine 2012b;107:233-41.

Acharya UR, Mookiah MR, Vinitha Sree S, Yanti R, Martis RJ, Saba L, Molinari F, Guerriero S, Suri JS. Evolutionary Algorithm-Based Classifier Parameter Tuning for Automatic Ovarian Cancer Tissue Characterization and Classification. Ultraschall Med 2012c;

Acharya UR, Sree SV, Krishnan MM, Molinari F, Saba L, Ho SY, Ahuja AT, Ho SC, Nicolaides A, Suri JS. Atherosclerotic risk stratification strategy for carotid arteries using texture-based features. Ultrasound in medicine & biology 2012d;38:899-915.

Acharya UR, Sree SV, Krishnan MM, Molinari F, Zieleznik W, Bardales RH, Witkowska A, Suri JS. Computer-aided diagnostic system for detection of Hashimoto thyroiditis on ultrasound images from a Polish population. Journal of ultrasound in medicine : official journal of the American Institute of Ultrasound in Medicine 2014a;33:245-53.

Acharya UR, Sree SV, Krishnan MM, Saba L, Molinari F, Guerriero S, Suri JS. Ovarian tumor characterization using 3D ultrasound. Technology in cancer research & treatment 2012e;11:543-52.

Acharya UR, Sree SV, Saba L, Molinari F, Guerriero S, Suri JS. Ovarian tumor characterization and classification using ultrasound-a new online paradigm. Journal of digital imaging 2013;26:544-53.

Acharya UR, Swapna G, Sree SV, Molinari F, Gupta S, Bardales RH, Witkowska A, Suri JS. A review on ultrasound-based thyroid cancer tissue characterization and automated classification. Technology in cancer research & treatment 2014b;13:289-301.

Acharya UR, Vinitha Sree S, Krishnan MM, Molinari F, Garberoglio R, Suri JS. Non-invasive automated 3D thyroid lesion classification in ultrasound: a class of ThyroScan systems. Ultrasonics 2012f;52:508-20.

Arts IM, Pillen S, Schelhaas HJ, Overeem S, Zwarts MJ. Normal values for quantitative muscle ultrasonography in adults. Muscle & nerve 2010;41:32-41.

Caresio C, Molinari F, Emanuel G, Minetto MA. Muscle echo intensity: reliability and conditioning factors. Clinical physiology and functional imaging 2014;

Chow RS, Medri MK, Martin DC, Leekam RN, Agur AM, McKee NH. Sonographic studies of human soleus and gastrocnemius muscle architecture: gender variability. European journal of applied physiology 2000;82:236-44.

Costanza MC, Afifi AA. Comparison of stopping rules in forward stepwise discriminant analysis. Journal of the American Statistical Association 1979;74:777-85.

Elias LJ, Bryden MP, Bulman-Fleming MB. Footedness is a better predictor than is handedness of emotional lateralization. Neuropsychologia 1998;36:37-43.

Fujikake T, Hart R, Nosaka K. Changes in B-mode ultrasound echo intensity following injection of bupivacaine hydrochloride to rat hind limb muscles in relation to histologic changes. Ultrasound in medicine & biology 2009;35:687-96.

Galloway MM. Texture analysis using gray level run lengths. Computer Graphics and Image Processing 1975;4:172-9.

Gao S, Peng Y, Guo H, Liu W, Gao T, Xu Y, Tang X. Texture analysis and classification of ultrasound liver images. Bio-medical materials and engineering 2014;24:1209-16.

Gdynia HJ, Muller HP, Ludolph AC, Koninger H, Huber R. Quantitative muscle ultrasound in neuromuscular disorders using the parameters 'intensity', 'entropy', and 'fractal dimension'.

European journal of neurology : the official journal of the European Federation of Neurological Societies 2009;16:1151-8.

Haralick RM, Shanmugam K, Dinstein IH. Textural Features for Image Classification. Systems, Man and Cybernetics, IEEE Transactions on 1973;SMC-3:610-21.

Kim N, Amin V, Wilson D, Rouse G, Udpa S. Ultrasound image texture analysis for characterizing intramuscular fat content of live beef cattle. Ultrasonic imaging 1998;20:191-205.

Maurits NM, Beenakker EA, van Schaik DE, Fock JM, van der Hoeven JH. Muscle ultrasound in children: normal values and application to neuromuscular disorders. Ultrasound in medicine & biology 2004;30:1017-27.

Maurits NM, Bollen AE, Windhausen A, De Jager AEJ, Van Der Hoeven JH. Muscle ultrasound analysis: normal values and differentiation between myopathies and neuropathies. Ultrasound in medicine & biology 2003;29:215-25.

Narici MV, Binzoni T, Hiltbrand E, Fasel J, Terrier F, Cerretelli P. In vivo human gastrocnemius architecture with changing joint angle at rest and during graded isometric contraction. The Journal of physiology 1996;496 (Pt 1):287-97.

Niu L, Qian M, Yang W, Meng L, Xiao Y, Wong KK, Abbott D, Liu X, Zheng H. Surface roughness detection of arteries via texture analysis of ultrasound images for early diagnosis of atherosclerosis. PloS one 2013;8:e76880.

Ojala T, Pietikäinen M, Harwood D. A comparative study of texture measures with classification based on featured distributions. Pattern Recognition 1996;29:51-9.

Ojala T, Pietikainen M, Maenpaa T. Multiresolution gray-scale and rotation invariant texture classification with local binary patterns. Pattern Analysis and Machine Intelligence, IEEE Transactions on 2002;24:971-87.

Pillen S, Arts IM, Zwarts MJ. Muscle ultrasound in neuromuscular disorders. Muscle & nerve 2008;37:679-93.

Pillen S, Tak RO, Zwarts MJ, Lammens MM, Verrijp KN, Arts IM, van der Laak JA, Hoogerbrugge PM, van Engelen BG, Verrips A. Skeletal muscle ultrasound: correlation between fibrous tissue and echo intensity. Ultrasound in medicine & biology 2009a;35:443-6.

Pillen S, van Alfen N. Skeletal muscle ultrasound. Neurological research 2011;33:1016-24.

Pillen S, van Dijk JP, Weijers G, Raijmann W, de Korte CL, Zwarts MJ. Quantitative gray-scale analysis in skeletal muscle ultrasound: a comparison study of two ultrasound devices. Muscle & nerve 2009b;39:781-6.

Radaelli R, Bottaro M, Wilhelm EN, Wagner DR, Pinto RS. Time course of strength and echo intensity recovery after resistance exercise in women. Journal of strength and conditioning research / National Strength & Conditioning Association 2012;26:2577-84.

Reeves ND, Maganaris CN, Narici MV. Ultrasonographic assessment of human skeletal muscle size. European journal of applied physiology 2004;91:116-8.

Singh A, Singh B. Texture Features Extraction in Mammograms Using Non-Shannon Entropies. In: Ao S-I, Rieger B, Amouzegar MA, ed. Machine Learning and Systems Engineering. Springer Netherlands, 2010. pp. 341-51.

Turo D, Otto P, Shah JP, Heimur J, Gebreab T, Zaazhoa M, Armstrong K, Gerber LH, Sikdar S. Ultrasonic characterization of the upper trapezius muscle in patients with chronic neck pain. Ultrasonic imaging 2013;35:173-87.

Walker FO, Cartwright MS, Wiesler ER, Caress J. Ultrasound of nerve and muscle. Clinical neurophysiology : official journal of the International Federation of Clinical Neurophysiology 2004;115:495-507.

Zaidman CM, Connolly AM, Malkus EC, Florence JM, Pestronk A. Quantitative ultrasound using backscatter analysis in Duchenne and Becker muscular dystrophy. Neuromuscular disorders : NMD 2010;20:805-9.

Zaidman CM, Holland MR, Anderson CC, Pestronk A. Calibrated quantitative ultrasound imaging of skeletal muscle using backscatter analysis. Muscle & nerve 2008;38:893-8.

Zaidman CM, Holland MR, Hughes MS. Quantitative ultrasound of skeletal muscle: reliable measurements of calibrated muscle backscatter from different ultrasound systems. Ultrasound in medicine & biology 2012;38:1618-25.

FIGURE CAPTIONS

Figure 1.

Region of interest (ROI) positioning in the transversal B-mode images: A) rectus femoris; B) vastus lateralis; C) tibialis anterior; D) medial gastrocnemius. The white arrows in panels A) and C) indicate, respectively, the central aponeurosis and the internal fascia that were never comprised into the ROI.

Figure 2.

Schematic representation of the computation of the Gray Level Co-occurrence Matrix (GLCM). A) Numerical values corresponding to the pixel intensities. B) Associated GLCM. C) Gray scale representation of the image in A). D) Gray scale representation of the GLCM. The red circles in A) depict the adjacencies (1,6), which correspond to the number circled in red in panel B).

Figure 3.

Schematic representation of the Local Binary Pattern (LBP) process. A) Original pixel intensities. B) Binarization by thresholding. C) Power-of-two weights. D) Final LBP neighborhood. The overall LBP value assigned to the central pixel is the sum of the numbers in D), which equals 216.

Figure 4.

Representation of the subjects in the plane of the first two canonical variables obtained by MANOVA. The features allowed for a clean-cut separation of the subjects on the basis of the gender. The full symbols represent the males (data from two male subjects are overlapped), the empty symbols the females.

Figure 5.

Distribution of the four most discriminant features for gender in the sample groups. The full symbols represent the males, the empty symbols the females. The red circles indicate the biceps brachii muscle, the down triangles the inferior ROI of the tibialis anterior. In each graph, the mean value and the interval corresponding to ± two standard deviations is represented. A) Haralick energy (along the angular direction θ = 135°). B) Haralick entropy (θ = 135°). C) Haralick correlation (θ = 90°). D) Local Binary Pattern (LBP) entropy.

Figure 6.

Representation of the subjects A) in the plane of the first two canonical variables, and B) in the plane of the first and third canonical variable obtained by MANOVA. Different symbols and colors are used for the different muscles. The full symbols represent the males, the empty symbols the females.

BB: biceps brachii; MG: medial gastrocnemius; VL: vastus lateralis; RF: rectus femoris; TA: tibialis anterior.

Figure 7.

Distribution of four discriminant features for muscle type in the sample groups. The full symbols represent the males, the empty symbols the females. In each graph, the mean value and the interval corresponding to ± two standard deviations is represented. A) Gray-level non-uniformity (GLNU, along the angular direction θ = 90°). B) Run length non-uniformity (RLNU, θ = 135°). C) Local Binary Pattern (LBP) entropy. D) Haralick entropy (θ = 135°).

Figure 8.

Results of the MANOVA analysis when only first order features are used to distinguish between genders and muscle types.

A) Representation of the subjects in function of the gender.

B) Representation of the subjects in function of the muscle type.

BB: biceps brachii; MG: medial gastrocnemius; VL: vastus lateralis; RF: rectus femoris; TA: tibialis anterior.

Figure 9.

Differences in mean echo intensity (first order feature) of four muscles between the two genders. The full symbols represent the males, the empty symbols the females. In each graph, the mean value and the interval corresponding to ± two standard deviations is represented.

APPENDIX

Haralick features

The Haralick features are based on the Gray Level Co-occurrence Matrix (GLCM). Let the image be represented by a $M \times N$ gray-scale matrix $I(x,y)$, where each element of the matrix indicates the intensity of a single pixel in the image. The co-occurrence matrix $C(i,j \mid \Delta x, \Delta y)$ is the second-order probability function estimation. This matrix denotes the rate of occurrence of a pixel pair with gray levels i and j, given the distances between the pixels are Δx and Δy in the x and y directions, respectively. The co-occurrence matrix $C(i, j \mid \Delta x, \Delta y)$ is defined as

$$C(i,j|\Delta x,\Delta y) = |\{(p,q),(p+\Delta x, q+\Delta y): I(p,q) = i, I(p+\Delta x, q+\Delta y) = j\}| \quad (1)$$

where $(p,q)(p+\Delta x, q+\Delta y) \in MxN$, $d = (\Delta x, \Delta y)$, and $|.|$ denotes the cardinality of a set. The probability that a gray level pixel i is at a distance $(\Delta x, \Delta y)$ away from the gray level pixel j is given by

$$P(i,j) = \frac{C(i,j)}{\sum C(i,j)} \quad (2)$$

An element of the GLCM matrix (i, j, d, θ) is defined as the joint probability of the gray levels i and j separated by distance d and along angular direction θ. To reduce the computation burden, we have considered θ as 0º, 45º, 90º, and 135º, and d is defined as the Manhattan or city block distance (*i.e.* the number of pixels that must be crossed) based on this GLCM (Haralick et al. 1973). These second order features are mathematically defined in Table 2.

Local Binary Pattern features

The LBP is computed by using the following method:

- A circular neighborhood of radius R pixels is considered around a pixel. The pixel is the center of the circular neighborhood and it has intensity equal to I_c.
- P points are chosen on the circumference of the circle with radius R such that they are all equidistant. Let I_p ($p = 1 \ldots P$) be the intensities of the P points on the circumference.

- These P pixels are converted into a circular bit-stream of zeros and ones according to whether the gray value of the pixel is less than or greater than I_c.

We considered P equal to 24 pixels and R equal to 3 pixels, in order to consider a relatively large neighborhood. The created neighborhood is then assigned with a uniformity measurement U that counts the number of bit transitions (from 0 to 1 and viceversa) in the circular domain (with reference to fig. 3, the U value would be equal to 4). We assigned to the LBP code only the patterns with $U \leq 2$, so that:

$$LBP(x) = \begin{cases} \sum_{p=1}^{P} s(I_p - I_c) & U(x) \leq 2 \\ P + 1 & otherwise \end{cases} \quad (3)$$

where $s(x)$ is the step function that equals 1 if $x \geq 0$ and is null for $x < 0$. Let's f_i be the relative frequency of the histogram derived from the LBP values of all the image pixels. The LBP energy is defined as:

$$LBP_{energy} = \sum_i f_i^2 \quad (4)$$

The LBP entropy can be defined as:

$$LBP_{entropy} = -\sum_i f_i \cdot log_2(f_i) \quad (5)$$

TABLES

Table 1

Mathematical description of first order statistical features. The input muscle region of interest (ROI) is denoted by *I(x,y).*

Feature	Description
Integrated optical density (IOD)	$IOD = \sum_{x=1}^{M} \sum_{y=1}^{N} I(x,y)$
Mean (m)	$m = \sum_{x=1}^{M} \sum_{y=1}^{N} \frac{I(x,y)}{M \times N}$
Standard deviation (σ)	$\sigma = \sqrt{\frac{\sum_{x=1}^{M} \sum_{y=1}^{N} \left\{ I(x,y) - m \right\}^2}{M \times N}}$
Variance (σ^2)	$\sigma^2 = \frac{\sum_{x=1}^{M} \sum_{y=1}^{N} \left\{ I(x,y) - m \right\}^2}{M \times N}$
Skewness (S_k)	$S_k = \frac{1}{M \times N} \frac{\sum_{x=1}^{M} \sum_{y=1}^{N} \left\{ I(x,y) - m \right\}^3}{\sigma^3}$
Kurtosis (K_t)	$K_t = \frac{1}{M \times N} \frac{\sum_{x=1}^{M} \sum_{y=1}^{N} \left\{ I(x,y) - m \right\}^4}{\sigma^4}$
Energy$_1$ (E_1)	$E_1 = \sum_{x=1}^{M} \sum_{y=1}^{N} I(x,y)^2$

Table 2

Mathematical description of the Haralick features.

Haralick feature	Description
Symmetry (I_{sym})	$I_{sym} = 1 - \sum_{i=0}^{N-1} \sum_{j=0}^{N-1} \lvert i-j \rvert P(i,j)$
Contrast (I_{con})	$I_{con} = \sum_{n=0}^{N-1} n^2 \left\{ \sum_{i=0}^{N} \sum_{j=0}^{N} P(i,j) \right\}$
Homogeneity (I_{hmg})	$I_{hmg} = \sum_{i=0}^{N-1} \sum_{j=0}^{N-1} \frac{1}{1+(i-j)^2} P(i,j)$
Entropy (I_{Entr})	$I_{Entr} = -\sum_{i=0}^{N-1} \sum_{j=0}^{N-1} P(i,j) \log(P(i,j))$
Energy (I_{Enrg})	$I_{Enrg} = \sum_{i=0}^{N-1} \sum_{j=0}^{N-1} P(i,j)^2$
Correlation* (I_{cor})	$I_{cor} = \frac{\sum_{i=0}^{N-1} \sum_{j=0}^{N-1} (i,j) P(i,j) - \mu_x \mu_y}{\sigma_x \sigma_y}$

* $\sigma_x, \sigma_y, \mu_x, \mu_y$ are the standard deviations and means of P_x, P_y which are the partial probability density functions. $p_x(i) = i^{th}$ entry in the marginal–probability matrix obtained by summing the rows of $P(i, j)$

Table 3

Mathematical description of the Galloway features. N_g represents the number of gray values in the image (*i.e.* the number of rows of the matrix *R*). N_r represents the number of runs (*i.e.* the number of columns of the *R* matrix).

Galloway feature	Description
Short run emphasis (SRE)	$SRE = \frac{\sum_{i=1}^{N_g}\sum_{j=1}^{N_r}\frac{R(i,j)}{j^2}}{\sum_{i=1}^{N_g}\sum_{j=1}^{N_r}R(i,j)}$
Long run emphasis (LRE)	$LRE = \frac{\sum_{i=1}^{N_g}\sum_{j=1}^{N_r}j^2 R(i,j)}{\sum_{i=1}^{N_g}\sum_{j=1}^{N_r}R(i,j)}$
Gray-level non-uniformity (GLNU)	$GLNU = \frac{\sum_{i=1}^{N_g}\left(\sum_{j=1}^{N_r}R(i,j)\right)^2}{\sum_{i=1}^{N_g}\sum_{j=1}^{N_r}R(i,j)}$
Run length non-uniformity (RLNU)	$RLNU = \frac{\sum_{j=1}^{N_r}\left(\sum_{i=1}^{N_g}R(i,j)\right)^2}{\sum_{i=1}^{N_g}\sum_{j=1}^{N_r}R(i,j)}$
Run percentage (RP)	$RP = \frac{\sum_{i=1}^{N_g}\sum_{j=1}^{N_r}R(i,j)}{N_g \cdot M_r}$

Table 4

Image features that are the most discriminant between the two genders and among the five muscles in the MANOVA analysis. The features are listed in order of decreasing weight in the MANOVA canonical variables.

LBP_{energy} - $LBP_{entropy}$: local binary pattern features; GLNU: gray-level non-uniformity; RLNU: run length non-uniformity; RP: run percentage; SRE: short run emphasis.

Most discriminant features for gender	Most discriminant features for muscle type
Haralick energy (θ = 0°, 45°, 90°, 135°)	GLNU (θ = 0°, 45°, 90°)
Haralick entropy (θ = 90°, 135°)	Haralick entropy (θ = 135°)
LBP_{energy}	$LBP_{entropy}$
Haralick correlation (θ = 45°, 90°)	RLNU (θ = 135°)
$LBP_{entropy}$	Haralick symmetry (θ = 90°)
	RP (θ = 90°)
	SRE (θ = 0°, 90°)

Table 5

Classification performance based on the 10 most significant features as obtained by the MANOVA analysis (leftmost half of the table) and based on the first order features (rightmost half of the table). AUROC indicates the area under the receiving-operator-curve.

	Ten most significant features			First order features only		
	Sensitivity (%)	Specificity (%)	AUROC	Sensitivity (%)	Specificity (%)	AUROC
BB	80.0	97.5	0.984	100	100	1
MG	85.0	98.3	0.990	50.0	95.0	0.932
VL	45.0	95.0	0.942	10.0	95.8	0.851
RF_{Med}	75.0	97.5	0.980	65.0	98.3	0.930
RF_{Lat}	50.0	95.8	0.936	45.0	95.8	0.910
TA_{Inf}	100	100	1	50.0	96.7	0.958
TA_{Sup}	100	100	1	5.0	99.2	0.765

BB: biceps brachii; MG: medial gastrocnemius; VL: vastus lateralis; RF_{Med} – RF_{Lat}: medial – lateral portion of the rectus femoris; TA_{Inf} - TA_{Sup}: inferior – superior portion of the tibialis anterior.

Figure 1

Click here to download high resolution image

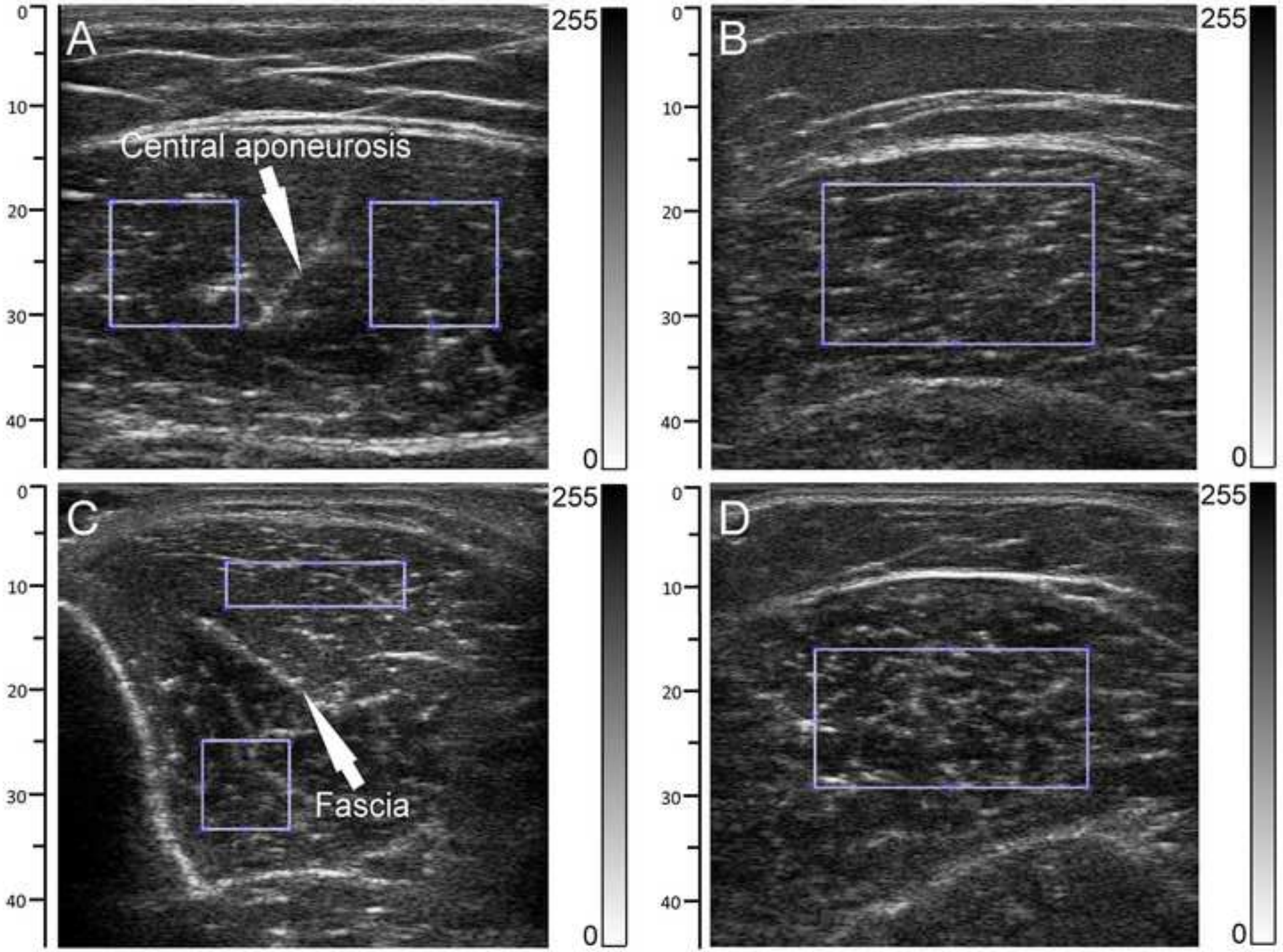

Figure 2

Click here to download Figure: fig2.eps

A

1	6	7	6	3
2	1	6	5	7
4	7	6	1	6
6	7	2	8	6
1	7	8	1	6

B

	1	2	3	4	5	6	7	8
1	0	0	0	0	0	4	1	0
2	1	0	0	0	0	0	0	1
3	0	0	0	0	0	0	0	0
4	0	0	0	0	0	0	1	0
5	0	0	0	0	0	0	1	0
6	1	0	1	0	1	0	2	0
7	0	1	0	0	0	2	0	1
8	1	0	0	0	0	1	0	0

C

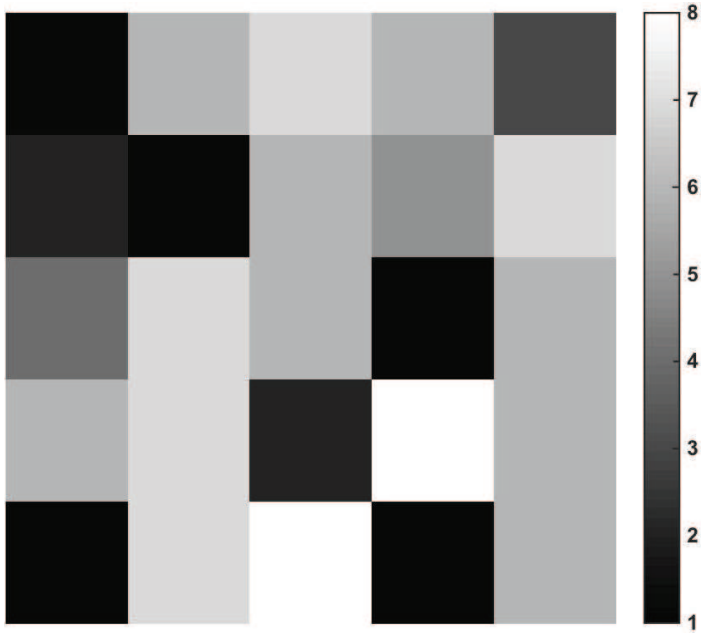

D

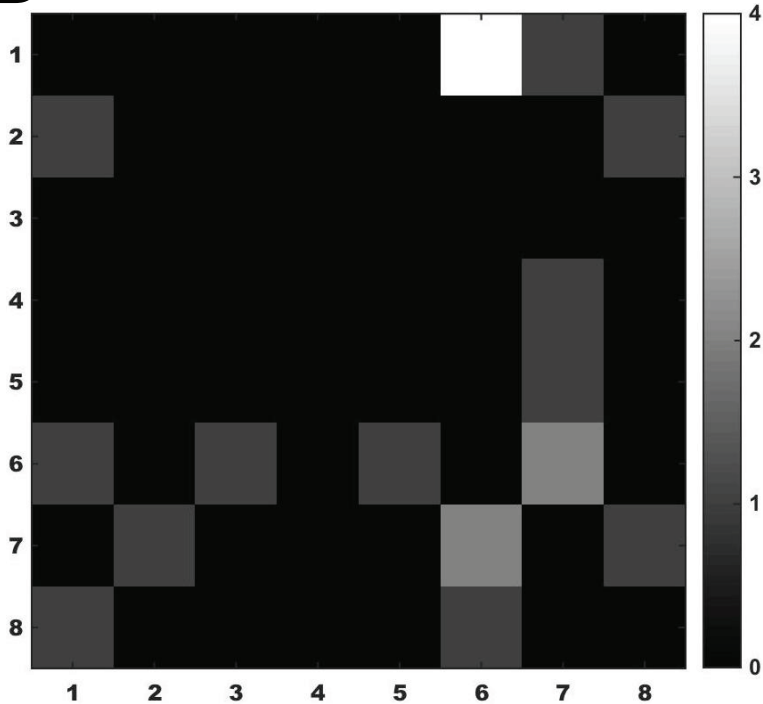

Figure 3
Click here to download Figure: fig3.eps

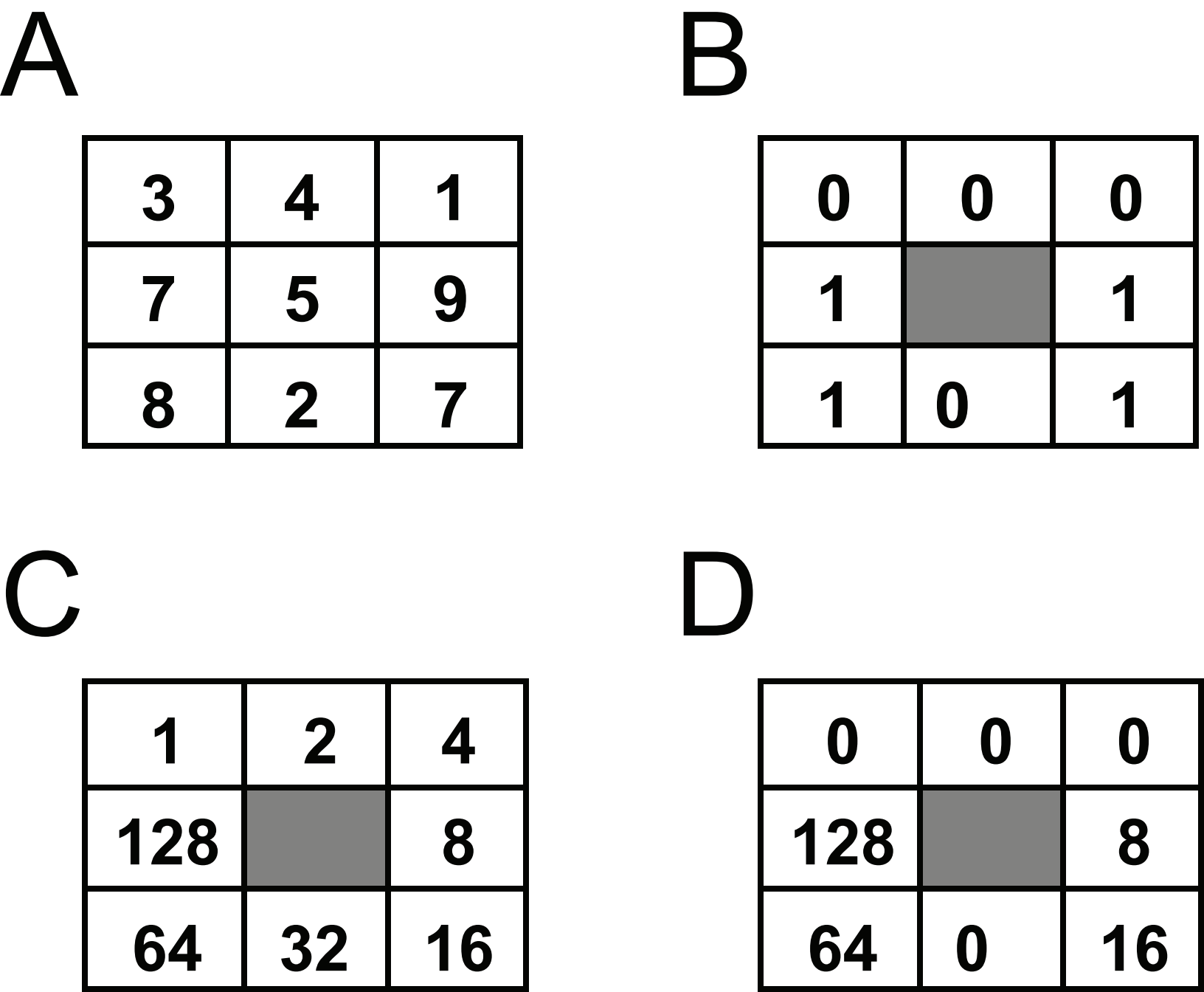

Figure 4

Click here to download Figure: fig4.eps

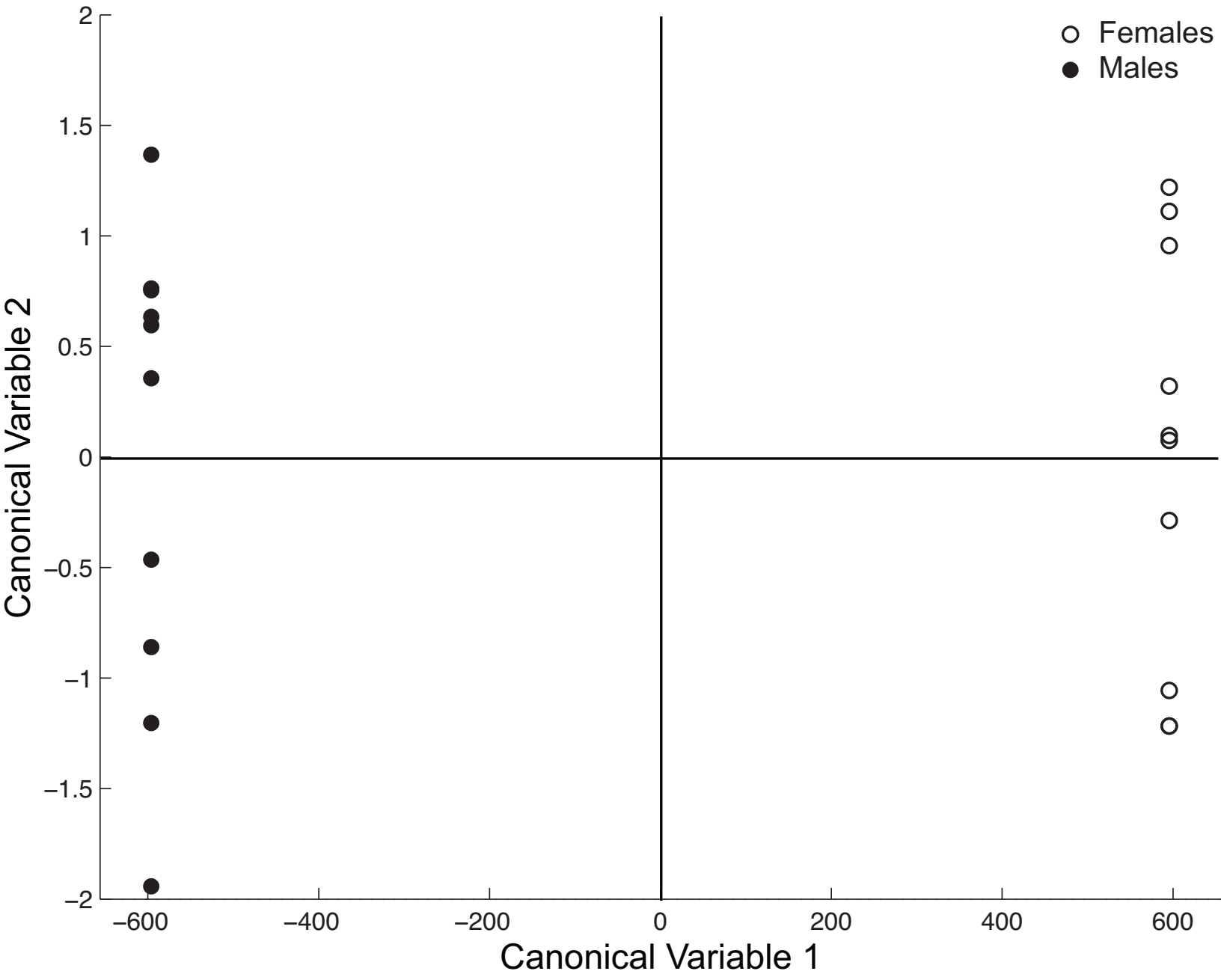

Figure 5

Click here to download Figure: fig5.eps

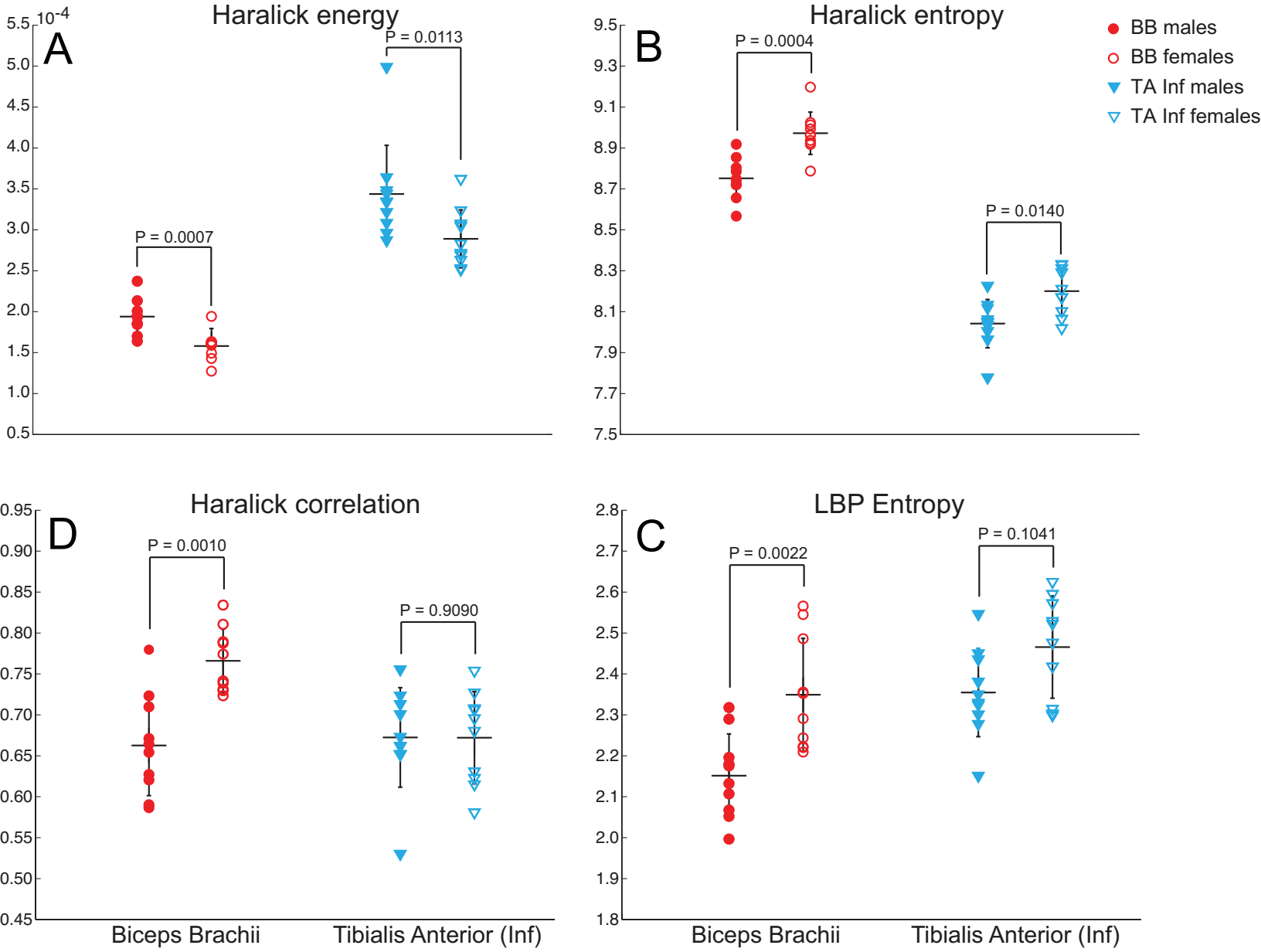

Figure 6

Click here to download Figure: fig6.eps

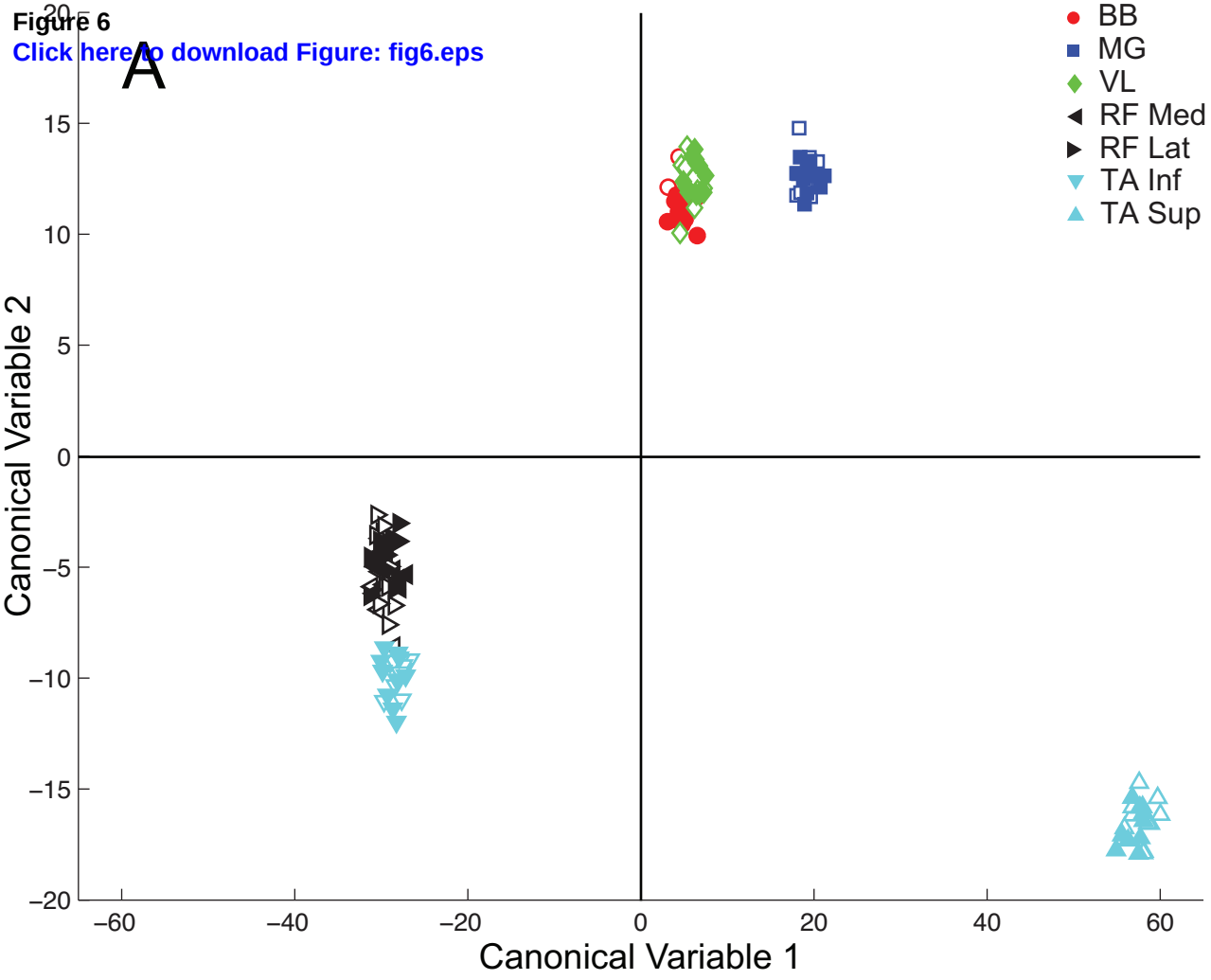

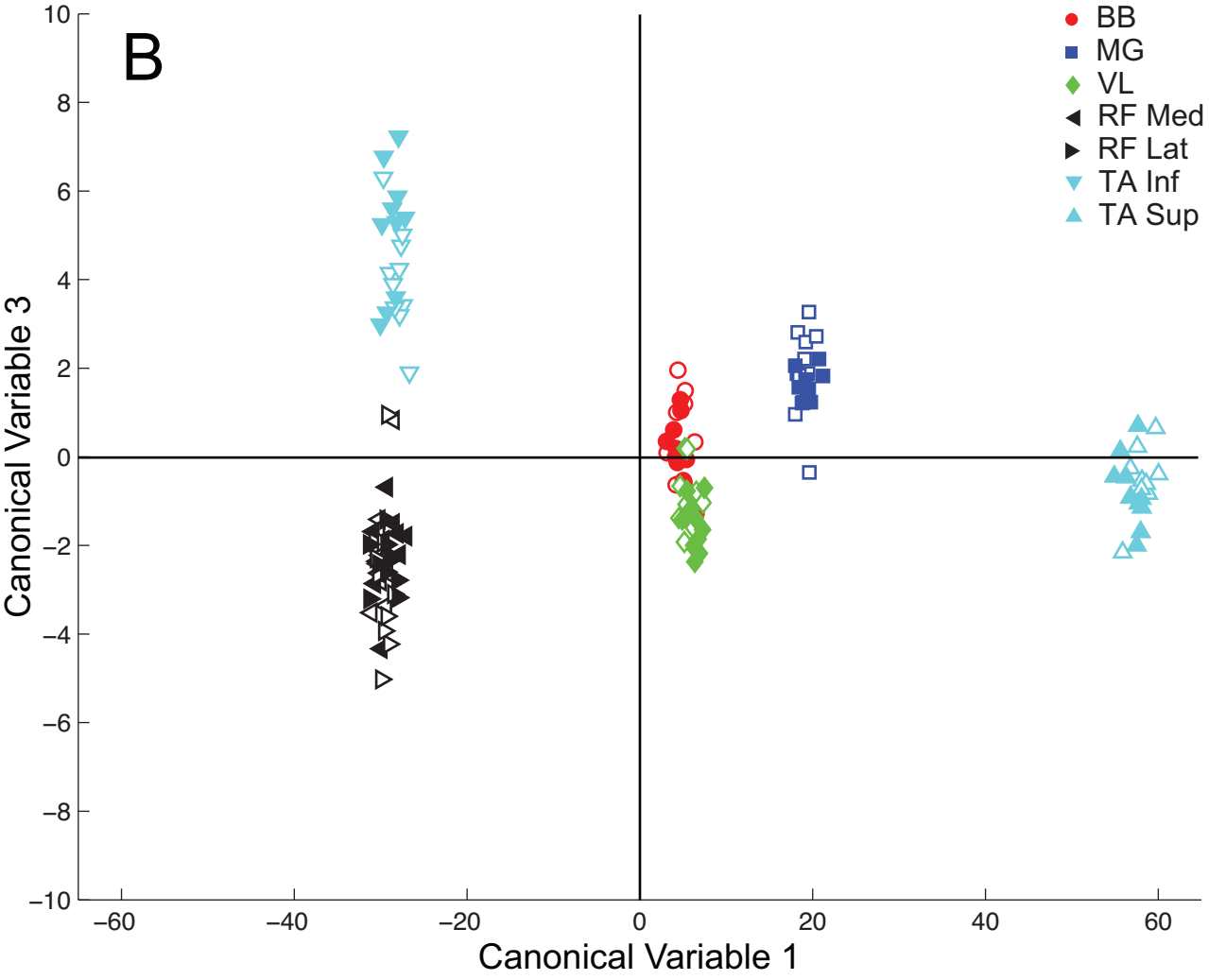

Figure 7

Click here to download Figure: fig7.eps

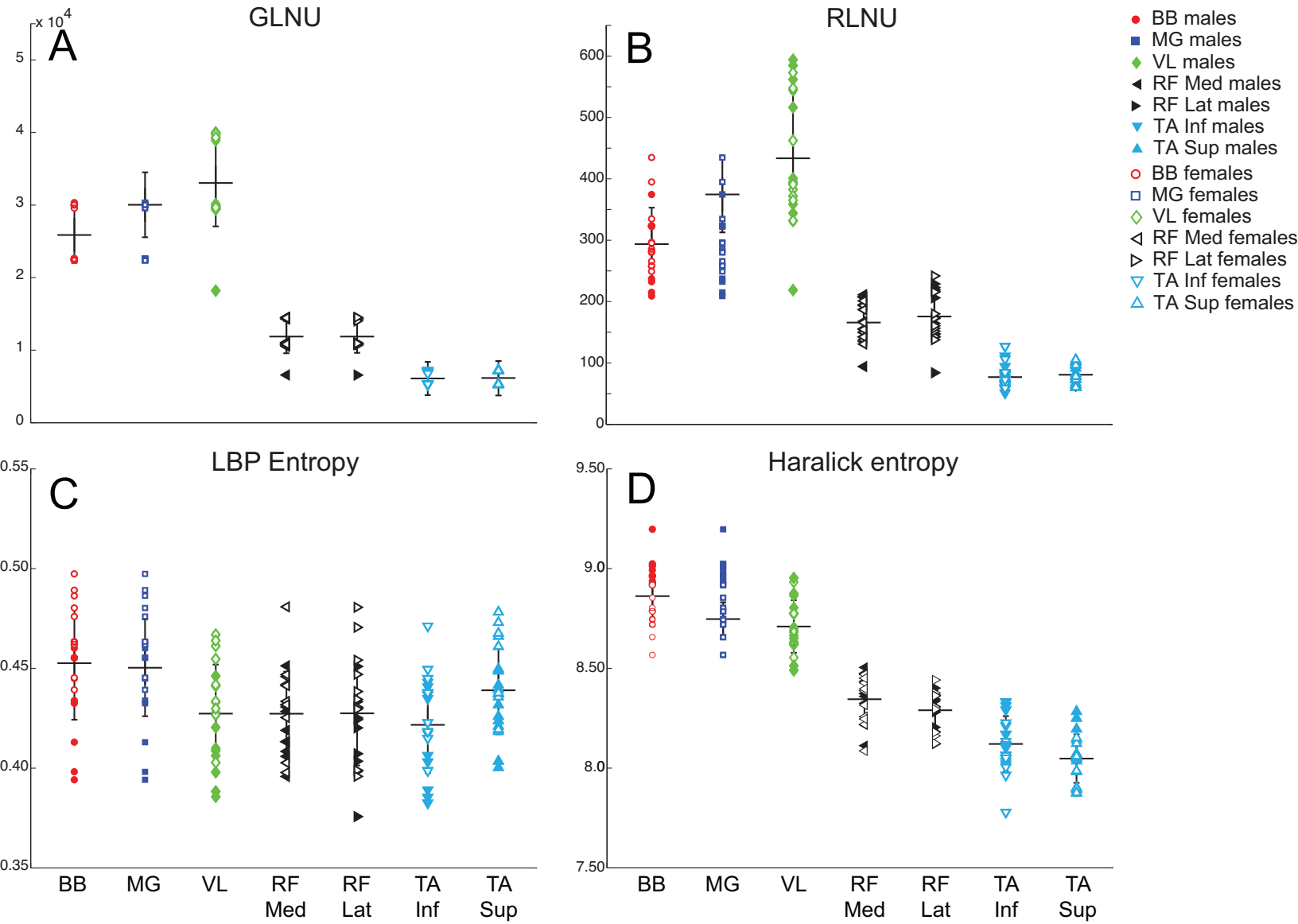

Figure 8

Click here to download Figure: fig8.eps

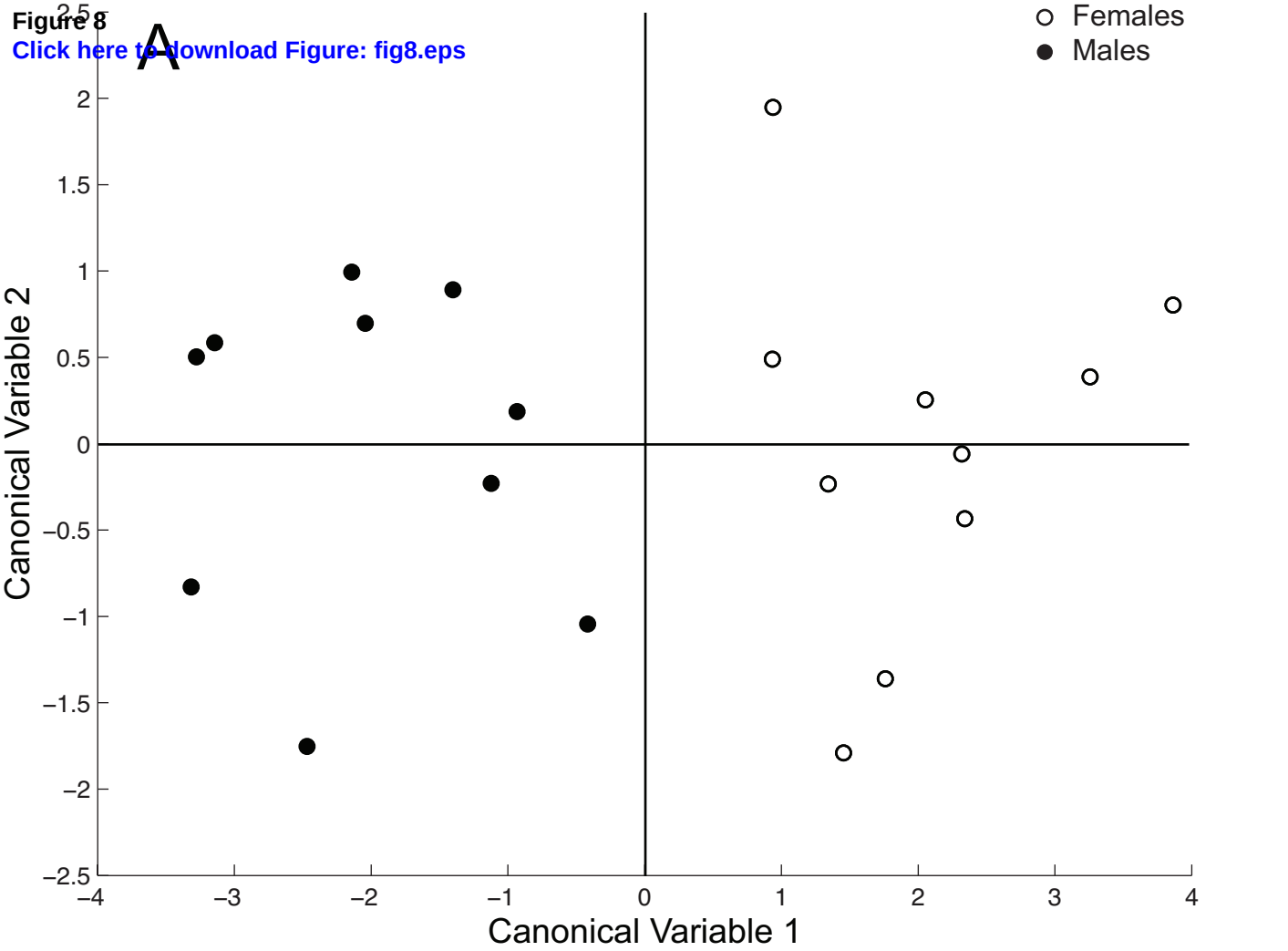

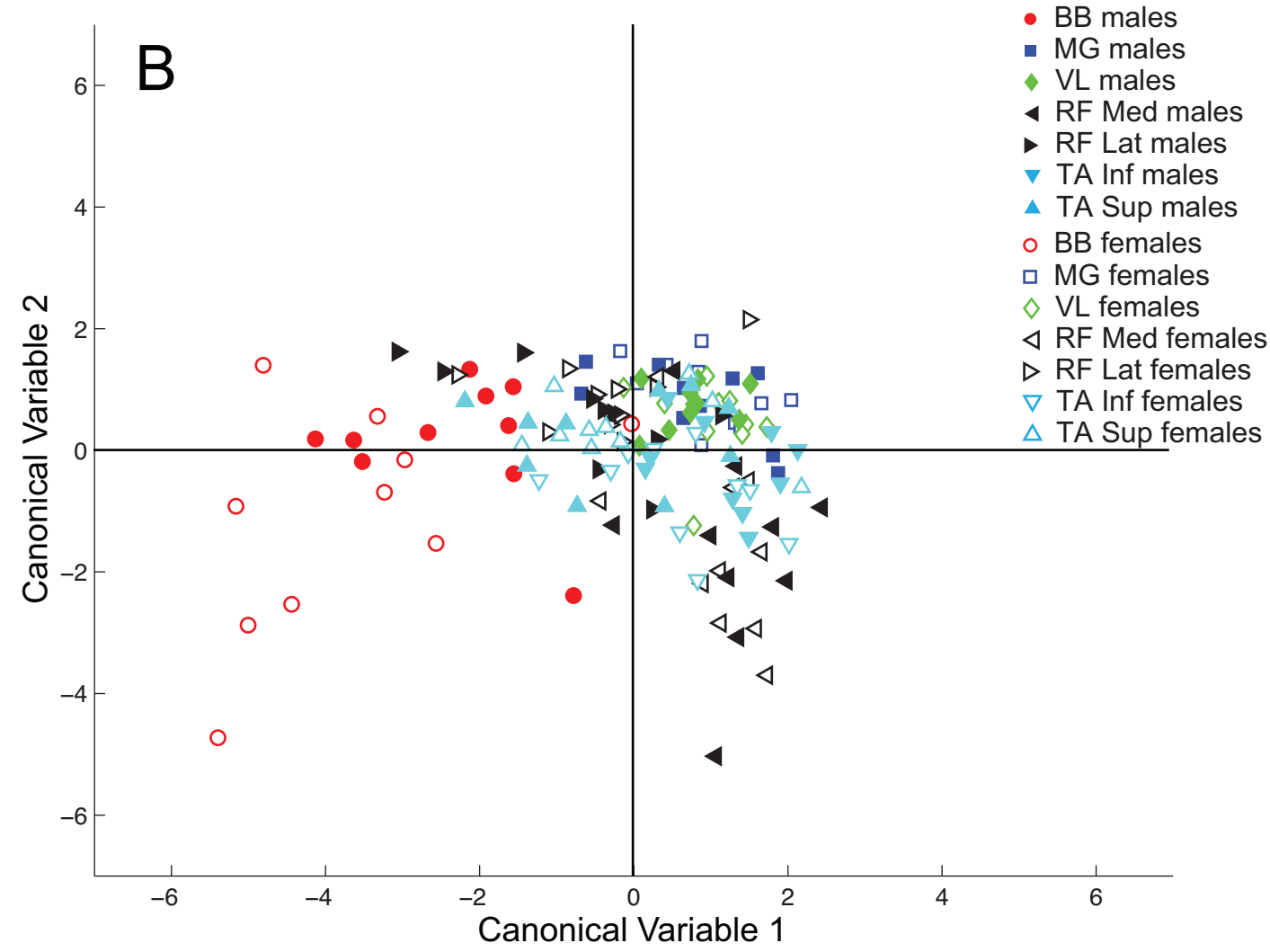

Figure 9

Click here to download Figure: fig9.eps